Site symmetry approach applied to the supercell model of $MgAl_2O_4$ spinel with oxygen interstitials: *Ab initio* calculations

Robert A. Evarestov[a*], Alexander Platonenko[b], Yuri F. Zhukovskii[b]

[a]*Institute of Chemistry, St. Petersburg State University, 198504 Petrodvorets, Russia*

[b]*Institute of Solid State Physics, University of Latvia, LV-1063 Riga, Latvia*

Abstract

In this study we simulate structural, electronic and phonon properties of $MgAl_2O_4$ spinel containing single oxygen interstitial (O_i) *per* crystalline *L*4 and *L*8 supercells, *e.g.*, its dumbbell configuration formed with one of the nearest regular oxygen atoms of the lattice (O_i-O_{reg}). Due to the splitting of the Wyckoff positions in supercell models of perfect crystal, five possible O_i positions with different site symmetry have been identified and studied (C_1, C_s, C_{3v} D_{2d} and T_d). First principles hybrid HSE06 DFT functional calculations on perfect and defective spinel structures have been accompanied by geometry optimization. The calculated properties of spinel crystal (lattice constants, bulk modulus, band gap as well as frequencies of infrared- and Raman-active vibrational modes) qualitatively well agree with the corresponding experimental data. The formation energy of O_i is found to be minimal for the interstitial site of lowest symmetry (C_1). The results obtained are important, in particular, for understanding the radiation and chemical stability as well as other key properties of $MgAl_2O_4$ spinel-type oxide crystals.

Keywords: $MgAl_2O_4$ spinel, point defect, oxygen interstitial, site symmetry, ab initio calculations

1. Introduction

Ternary spinel-type AB_2O_4 oxides known and studied for a long time enough [1-3] belong to a class of advanced compounds with various electrical, magnetic and optical properties. Spinel-structured magnesium aluminate ($MgAl_2O_4$), both single-crystalline and ceramic, characterized by cubic close-packed spatial crystalline morphology, possesses high transparency from visible to infrared wavelength range, enhanced strength and melting temperature, excellent chemical and radiation resistance as well as low electrical losses [4-6]. Combination of these properties makes magnesium aluminate suitable for a number of technological applications, although all of them require to consider influence of $MgAl_2O_4$ structural defects on the corresponding processes: (*i*) involvement in construction of fusion and fission reactors (inert matrices for nuclear fuels [7], transparent radio-frequency windows for fusion reactors [8], *etc.*) where spinel demonstrates remarkable resistance to formation of structural damages caused by neutrons and light ions, *e.g.*, amorphous microareas inside $MgAl_2O_4$ lattice, which essentially weaken further penetration of irradiation; (*ii*) defective spinel crystals, colored or colorless, in dependence on what kind of point defects is prevailing in them (neutral or charged vacancies, native interstitials and anti-sites, impurity substitutes, pair-wise defects, *etc.*), used in different electronic and optical devices [9-11] (as to irradiation in the range of visible spectrum, just presence of *F* centers is mainly responsible for it); (*iii*) supporting material for catalytic reactions possessing long-term durability [12, 13] (it was found that oxygen vacancies at its surface layers of support play prominent role in dispersion of catalytic metal nanoclusters, their migration and stabilization); (*iv*) thin films of Mg-spinel used in humidity-measured devices [14].

*e-mail address: r.evarestov@spbu.ru

Essential theoretical efforts have been undertaken aiming to properly describe the equilibrium geometry and electronic structure as well as chemical and physical (*e.g.*, elastic) properties of $MgAl_2O_4$ bulk in absence of any types of structural defects [15-19] performing for this purpose mainly first principles calculations (within either plane-wave methods [15-17] or Gaussian-type orbital formalism [18]) as well as force-field simulations [19].

Much more attention was paid so far to clarify theoretically how point defects and their aggregates influence the structural, electronic and optical properties of $MgAl_2O_4$ and related ternary compounds [20-26]. According to systematic studies of defective $MgAl_2O_4$, a presence of native defects can promote important changes in those properties [20]. The formation energies of various isolated defects in the most stable charge states were calculated for: (*i*), the vacancies of magnesium (V_{Mg}), aluminum (V_{Al}) and oxygen (V_O); (*ii*) oxygen interstitial (O_i), (*iii*) magnesium and aluminum anti-sites (Mg_{Al} and Al_{Mg}), (*iv*) some complex defects (V_O+O_i, V_O+Al_{Mg}, V_O+Mg_{Al}, Mg_{Al}+Al_{Mg}, *etc.*). It was concluded that anion vacancies can adequately compensate the observed deficit of positive charges. Radiation-induced damages in magnesium aluminate spinel were studied in Ref. [21]: for this aim, molecular dynamics of collision cascades in spinel were performed, in order to determine both the threshold displacement energies and the damage inflicted to the lattice. Density Functional Theory (DFT) plane wave simulations of thermodynamic properties have been performed to study substitutes of isolated cations and oxygen vacancies in Mg-spinel [22]. The calculated formation enthalpy of magnesium cation substituted by Ca, Cu, and Zn ions indicated that transition metal dopants are energetically stable in $MgAl_2O_4$ bulk at low oxygen chemical potential. In order to examine defect production and stability in spinel structures, defect kinetics was considered [23]. It was described for three spinel oxides: $MgAl_2O_4$, $MgGa_2O_4$, and $MgIn_2O_4$ using temperature accelerated dynamics (TAD), which revealed varying tendencies to disorder the cation sublattices. In order to study the influence that anti-site cation defects have on the populations of other intrinsic defects [24], those are associated with Schottky and Frenkel reactions. Point and small cluster defects in $MgAl_2O_4$ bulk spinel were also studied from *ab initio* viewpoint [25]. As favorable point defects considered during simulations of collision cascade the following ones were chosen: (*i*) cation anti-site defects possessing small formation energy and high stability; (*ii*) both O and Mg split interstitials and vacancies; (*iii*) isolated Al interstitials, on the other hand, were found to be energetically unfavorable. Large-scale *ab initio* defect calculations performed on a large number of spinel oxides revealed the major trends controlling their doping ability were uncovered [26]. Anti-site defects were described as the main source of electrical conductivity in these compounds. On the whole, in spite of undertaken efforts, a number of properties of both perfect and defective spinel-type $MgAl_2O_4$ bulk are not yet completely clear.

Traditional approach to aforementioned supercell models of the defective crystals usually begins with arrangement of point defect (*e.g.*, O_i interstitial) at position possessing the highest site symmetry. However, our recent simulations of oxygen atom interstitial in various supercells of binary oxide α-Al_2O_3 crystal the calculated formation energy of O_i has been found to be the minimal for the interstitial site of the lowest symmetry (C_1) [27]. The latter has been found to be unstable with respect to the low-barrier transformation into split interstitials (dumbbells between them and their nearest regular oxygens O_i-O_{reg}) with an energy gain of 2.5 eV. Obviously, oxygen interstitial transport in corundum can be controlled by the dumbbell bond breaking and re-

forming. According to earlier simulations, O_i atoms tend to form split interstitials with regular oxygen ions in binary MgO oxide as well [28].

The purpose of our current study is to apply site symmetry formalism for better understanding of O_i interstitial behavior in different supercell configurations of $MgAl_2O_4$ bulk (including possibility of its inter-lattice migration). The contents of the current paper is organized as the following: in Section 2, we adapt the formalism of site symmetry approach for O_i interstitials in Mg-spinel crystal; in Section 3, we describe computational scheme of *ab initio* hybrid DFT-LCAO calculations using HSE06 functional on perfect and defective $MgAl_2O_4$ spinel structures as well as their electronic and phonon properties; analysis of obtained results is given in Section 4, while the most important conclusions are formulated in Section 5.

2. Site symmetry approach to oxygen interstitials in spinel structure

The symmetry of $MgAl_2O_4$ spinel structure is described by non-symmorphic space group 227 $Fd\bar{3}m$ with face-centered cubic (*fcc*) lattice, the primitive unit cell of which (Fig. 1a) includes two formula units (14 atoms). For origin choice 2 in this space group description [29], atoms in spinel structure are distributed over Wyckoff positions by the following way. Mg and Al atoms occupy Wyckoff positions 8*a* ($^1/_8$ $^1/_8$ $^1/_8$) and 16*d* ($^1/_2$ $^1/_2$ $^1/_2$), corresponding to site symmetry groups *S*24 (space groups $\bar{4}3m$ *vs.* Schoenflies' point group T_d) as well as *S*12 ($\bar{3}m$ *vs.* D_{3d}), respectively. O atoms occupy Wyckoff positions 32*e* (x x x) with one free parameter *x* and site symmetry groups *S*6 ($3m$ *vs.* C_{3v}). The multiplicity of Wyckoff positions are given here and in what follows for conventional (cubic) unit cell which consists of four primitive unit cells, *i.e.*, 8 formula units of $MgAl_2O_4$ spinel crystal (Fig. 1). We use in this study designation *SP* for the site symmetry point group, consisting of *P* point symmetry operations.

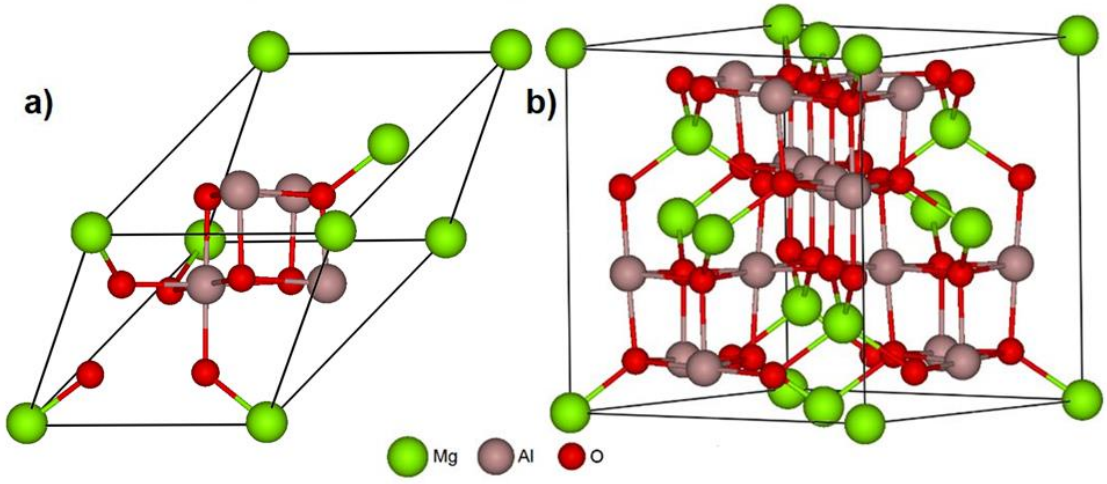

Figure 1. Axonometric views of 14-atom *L*1 primitive unit cell (a) and 56-atom *L*4 conventional unit cell (b) of cubic-structured defect-less $MgAl_2O_4$ spinel bulk. Small red balls, middle-sized brown-gray balls and large light-green balls image O, Al and Mg atoms, respectively. Lattice parameter a_0 of Mg-spinel lattice corresponds to the length of cubic edge between the two external Mg atoms located at apexes (b).

For the oxygen interstitial in spinel structure any of the following vacant Wyckoff positions could be used as an initial position in geometry optimization calculations: a) two positions being parameter free - 8*b* ($^3/_8$ $^3/_8$ $^3/_8$) and 16*c* (0 0 0) with site symmetries *S*24 ($\bar{4}3m$ *vs.* T_d) and *S*12 ($\bar{3}m$ *vs.* D_{3d}), respectively; b) one parameter dependent positions 48*f* (x $^1/_8$ $^1/_8$) and 96*h* (0 y $-y$) with

site symmetries *S*4 ($2mm$ *vs.* C_{2v}) and *S*2 (2 *vs.* C_2), respectively; c) two parameter dependent positions 96*g* ($x\ x\ z$) with site symmetry *S*2 (m *vs.* C_s) and general three parameter dependent position ($x\ y\ z$) with site symmetry *S*1 (1 *vs.* C_1). Due to the undefined values of all the parameters contained in vacant Wyckoff positions we place the interstitial oxygen in parameter free positions 8*b* or 16*c* and model the defective crystal within Supercell model (SCM) [30].

Defining $\boldsymbol{a}_i(\Gamma_1)$ (i = 1, 2, 3) as the basic translation vectors of the initial direct Bravais lattice of type Γ_1 while $\boldsymbol{A}_j(\Gamma_2)$ (j = 1, 2, 3) as the basic translation vectors of the new Bravais lattice of type Γ_2 with the same point symmetry but composed of supercells, we can express the latter as:

$$\boldsymbol{A_j}(\Gamma_2) = \sum_i l_{ji}(\Gamma_2\Gamma_1)\boldsymbol{a_i}(\Gamma_1) \qquad |\det l| = L, \tag{1}$$

where $l_{ji}(\Gamma_2\ \Gamma_1)$ are integer elements of the matrix $l(\Gamma_2\ \Gamma_1)$ defining the transition from the lattice of type Γ_1 to the lattice of type Γ_2. L is the number of primitive unit cells in the supercell. We consider here two supercell transformation matrices:

$$\begin{bmatrix} -1 & 1 & 1 \\ 1 & -1 & 1 \\ 1 & 1 & -1 \end{bmatrix}, \quad L = 4 \tag{2}$$

and

$$\begin{bmatrix} 2 & 0 & 0 \\ 0 & 2 & 0 \\ 0 & 0 & 2 \end{bmatrix}, \quad L = 8 \tag{3}$$

Matrix (2) transforms the initial face centered cubic lattice to a simple cubic lattice *i.e.*, the corresponding supercell is already mentioned as conventional cell for face centered cubic lattice. This supercell consists of 8 $MgAl_2O_4$ formula units (Figure 1), *i.e.,* 56 atoms.

Transformation (3) with diagonal matrix maintains the lattice type increasing twice the primitive unit cell translation vectors. The corresponding supercell consists of 16 $MgAl_2O_4$ formula units, *i.e.*, 112 atoms. Both supercell transformations (2) and (3) maintain the cubic point symmetry of the lattice. The interstitial atom in the traditional for SCM approach is placed to the vacant Wyckoff position with the highest possible site symmetry. In our case it is vacant Wyckoff position 8*b* with the site symmetry *S*24 (T_d). By our opinion, this approach was used in the first principles supercell calculations [27] but, unfortunately, the details of the interstitial oxygen position choice are not given in that publication.

In the SCM models interstitial oxygen is periodically repeated. Point defects are placed occupying position with the site symmetry *SP*. The perfect spinel crystal possesses the symmetry of space group $G = Fd\bar{3}m = T_dF$ where T_d is the translation subgroup (formed by face centered cubic lattice basic translations), $F = G/T_d = O_h$.

Supercell model of the defective crystal is described by a space group $G_d = T_AF_d$, where G_d, T_A and F_d are subgroups of G, T_A and F, respectively. In the primitive unit cell the parameter-free vacant Wyckoff positions 8*b* and 16*c* have point symmetry T_d and D_{3d}, respectively. The symmetry groups G_d, T_d and F_d of defective crystal are defined by the SCM model choice and can be determined using new computer tools and programs available at the Bilbao Crystallographic Server (BCS) [29]. BCS CELLSUB program allows one to obtain subgroups of each space group for a given *t*-index defining the multiplication of the cell (t = 4 or 8 for transformations (2) or (3), respectively).

Using CELLSUB program of BCS server, one finds the space groups $G_d = T_A F_d$ for two supercells defined by transformations (2) and (3). These space groups are symmorphic: $P\bar{4}3m$ (215) for supercell transformation (2) and $F\bar{4}3m$ (216) for supercell transformation (3). The WYCKSPLIT program from the Bilbao Crystallographic Server has been used here too, to find the splitting of vacant Wyckoff positions 8*b* and 16c in the perfect crystal for chosen supercells *L*4 and *L*8.

For the group-subgroup chain 227($Fd\bar{3}m$) > 215 ($P\bar{4}3m$), *i.e.*, *L*4 supercell:

8*b* (group 227) = 1*b*3*d*4*e* (group 215); 16*c* (group 227) = 4*e*12*i* (group 215). (4)

For the group-subgroup chain 227($Fd\bar{3}m$) > 216 ($F\bar{4}3m$), *i.e.*, *L*8 supercell:

8*b* (group 227) = 4*c*4*d*16*e*16*e*24*f* (group 216);

16*c* (group 227) = 16*e*16*e*48*h*48*h* (group 216). (5)

The point symmetry of the groups 215 and 216 Wyckoff positions is the following [29]:

Group 215: *S*24(T_d) - 1*b*(½ ½ ½), *S*8(D_{2d}) - 3*d*(½ 0 0), *S*6(C_{3v}) - 4*e*(*x x x*) and *S*2(C_s) - 12*i*(*x x z*) (6)

Group 216: *S*24(T_d) - 4*c*(¼ ¼ ¼), 4*d*(-¼ -¼ -¼), *S*6(C_{3v}) - 16*e*(*x x x*), *S*4(C_{2v}) - 24*f*(*x* ¼ ¼) and *S*2(C_s) - 48*h*(*x x z*). (7)

It is seen that in the split Wyckoff positions appear those containing one and two free parameters. Placing interstitial oxygen in these positions during geometry optimization gives possibility to find optimized values of these parameters and thus lower the total energy in the supercell calculations.

Thus, when inserting interstitial atoms in Wyckoff positions possessing different site symmetry (Figure 2), we observe different defect configurations and different formation energies after the structure relaxation.

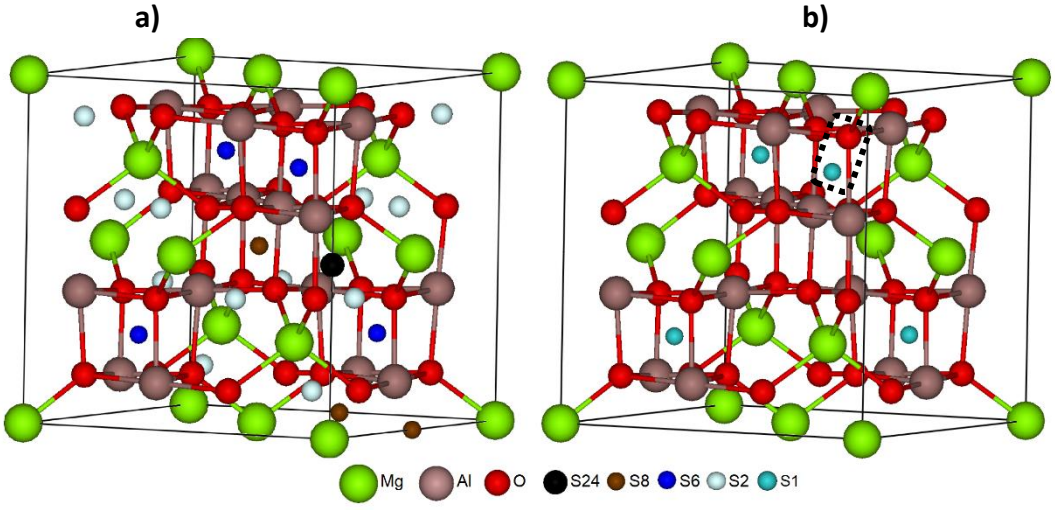

Figure 2. Axonometric view of *L*4 conventional unit cell for $MgAl_2O_4$ spinel bulk. Graphical images of O, Al and Mg atoms are the same as described in Figure 1: (a) labelled positions of site symmetry imaged by smallest balls of different colors are designated as *S*24, *S*8, *S*6 and *S*2; (b) interstitial *S*1 sites occupy the same positions as *S*6 ones but after total distortion of their symmetry (C_1) while dotted rectangles show dumbbell orientations.

The results of oxygen interstitial calculations in two supercells *L*4 and *L*8 (the latter is determined *via* *L*1 by 2x2x2 extension) for two different split Wyckoff positions are analyzed in the Section 4.

3. Computational details

3.1. Calculations of the atomic and electronic structure

Majority of first principles simulations on Mg-spinel described so far (Section 1) has been performed within the formalism of spin-polarized DFT method based on plane waves approach

(DFT-PW). We have found only one paper presenting results of alternative DFT calculations on the electronic structure of $MgAl_2O_4$ within the formalism of linear combination of atomic orbitals (LCAO) [15]. Nevertheless, Mg-spinel crystal containing interstitial oxygen atom O_i *per* supercell of various configurations has been calculated by us using the DFT-LCAO method within the formalism of HSE06 hybrid exchange-correlation functional [31] as implemented in CRYSTAL14 package [32]. To our mind, this methodology better corresponds to the proper description of interatomic bonding and electron charge distribution in crystal. We have used the all-valence basis set (BS) of atomic Gaussian type functions (GTFs) both for O atoms constructed using pure *s*- and *d*- as well as hybrid *sp*-AOs in the form of 6*s*-2111*sp*-1*d* as described elsewhere [33] as well for Mg atoms (8*s*-511*sp*-1*d*) [34]. Alternatively, the effective core pseudopotential (ECP) with 3*s*23*p*1*d* external shell has been developed for Al atoms [35] and used by us in this study.

For the integration within the reciprocal lattice, sampling the Brillouin zone (BZ) with the chosen 4×4×4 Monkhorst-Pack mesh [36] provides a balanced summation in both direct and reciprocal space of 56 atom supercell (Figure 1b). First principles Self-Consistent Field (SCF) calculations have been considered as converged only when the total energy differs by less than 10^{-7} a.u. in two successive SCF cycles [32]. The initial geometry has been optimized by keeping the corresponding bulk symmetry fixed. Within the self-consistency, the accuracies (tolerances) 10^{-7}, 10^{-8}, 10^{-7}, 10^{-7}, 10^{-14} have been chosen for calculations of Coulomb and exchange integrals [32]. The calculated values of lattice constant a_0 of the cubic-structured $MgAl_2O_4$ bulk (Fig. 1) and free parameter *u* describing arrangement of oxygen atoms in the lattice derived from formula for the distance between the nearest Mg and O atoms $r_{\mathrm{Mg-O}}^{min} = a_o\sqrt{3(u-\frac{1}{8})}$ [37] are well consistent with the corresponding experimental data (Table 1).

Table 1 Calculated and experimental properties of Mg-spinel

$MgAl_2O_4$ bulk	Hamiltonian HSE06	experiment
lattice constant a_o, Å	8.064	8.081 [38]
free parameter *u*	0.2635	0.2623 [38]
band gap $\Delta\varepsilon_{gap}$, eV	8.79	7.80 [39]
bulk modulus *B*, GPa	211	197 [40]

Good qualitative agreement is also achieved between the corresponding values of the band gap $\Delta\varepsilon_{gap}$ derived from the one-electron energy spectrum $\varepsilon(\varepsilon_i)$ as well as bulk modulus *B* evaluated as the first numerical derivatives of analytical energy gradients by varying the lattice constant and fitting the dependence *E*(*V*) of the total energy *per* unit cell on its volume truncated to a second order of polynomial energy fit (in harmonic approximation): $B = \frac{2}{9V}(\frac{\partial^2 E}{\partial\epsilon_1^2} + 2\frac{\partial^2 E}{\partial\epsilon_1\partial\epsilon_2})$, where ϵ_1 and ϵ_2 are the elements of elastic matrix [32] (Table 1). The computational scheme selected by us demonstrates high accuracy in reproducing basic properties of bulk spinel crystal. Additionally, the effective charges on atoms of Mg-spinel and bond populations between them, which are problematically to measure experimentally, have been estimated using Mulliken population analysis [41]. In this study, all first principles calculations have been performed in this study using the total geometry optimization of both perfect and O_i interstitial-containing $MgAl_2O_4$ bulk.

To evaluate the formation energy *per* $MgAl_2O_4$ conventional unit cell for O_i interstitial in different spinel lattice symmetry sites (Fig. 2), we have applied expression similar to that used for description of symmetry sites for O_i-containing interstitials in corundum bulk [28]:

$$E_{form}^{O_i} = E_{total}^{MgAl_2O_4(O_i)} - E_{total}^{MgAl_2O_4(perfect)} - \frac{1}{2}E_{total}^{O_2}, \quad (8)$$

where $E_{total}^{MgAl_2O_4(O_i)}$ is the total electronic energy of the conventional spinel unit cell containing O_i interstitial, $E_{total}^{MgAl_2O_4(perfect)}$ the total electronic energy of a perfect unit cell, and $E_{total}^{O_2}$ the total electronic energy of oxygen molecule. Analogously, the magnitude of $E_{form}^{O_i}$ markedly depends on the site symmetry of interstitial oxygen atom (Table 2) as discussed in Section 4.

3.2. Calculations of the phonon structure

For phonon calculations, we use harmonic approach and direct frozen phonon method realized in CRYSTAL14 code [42-45]. LO (longitudinal optical) – TO (transverse optical) splitting, *i.e.*, the shift in frequency between the LO and TO phonons at the Brillouin zone center, has been calculated using CRYSTAL14 code [32] with experimental value of high-frequency dielectric constant ε = 2.89 taken from Ref. [18]. To perform calculations of vibrational frequencies, using frozen phonon method (direct method), SCF convergence has been set to 10^{-9} a.u. [32].

The perfect $MgAl_2O_4$ spinel crystal with 14 atoms in a primitive unit cell (Figure 1a) possesses the following symmetry types of vibrational modes at Γ point of the Brillouin zone (the size of mechanical representation is 42):

$$\Gamma_{vib} = A_{1g} + 2A_{2u} + E_g + 2E_u + T_{1g} + 5T_{1u} + 3T_{2g} + 2T_{2u} \quad (9)$$

This result is found taking into account the occupation of Wyckoff positions in primitive unit cell of Mg-spinel crystal using SITESYM program [29]. One of T_{1u} modes is acoustic one with zero frequency at Γ point. There are five modes (A_{1g}, E_g, $3T_{2g}$), which are Raman-active, and four T_{1u} modes, which are infrared-active. Seven modes ($2A_{2u}$, $2E_u$, T_{1g}, $2T_{2u}$) are silent *i.e.*, non-visible in the vibrational spectra of $MgAl_2O_4$ crystal. Table 3 in Section 4 gives the frequencies of the optical modes of Mg-spinel at Γ point of BZ for the primitive unit cell (LO phonon frequencies are given in brackets). A good agreement is established between the frequencies of spinel bulk optical modes calculated by two different methods: DFT-PW LDA calculations [45] and our hybrid DFT-LCAO HSE06 calculations. The experimental data used for verification are taken from [46] for Raman-active modes and from [47] for infrared-active modes and are in reasonable agreement with the theoretical data.

4. Results and discussion

4.1. O_i interstitial formation energy and electronic structure *versus* spinel site symmetry

The results of hybrid spin-polarized HSE06 calculations of O_i interstitials located inside 5 spinel sites of different symmetry (*S*24, *S*8, *S*6, *S*2, and *S*1) when considering two types of supercells (*L*4 and *L*8) are systematized in Table 2. All results correspond to zero total spin of the system. Formation energies vary from 13.7 eV (for highest *S*24 site-symmetry position) down to 2.31 eV (for non-symmetric *S*1 configuration arising after total symmetry removal from *S*6 site).

*S*24 and *S*8 site symmetries of $MgAl_2O_4$ bulk (Fig 2) give very close calculated results (Table 2) since their high symmetry structure relaxations are insignificant while large 1NN and 2NN distances are qualitatively close for both symmetry sites and supercell sizes, which leads to a high formation energy of defect. *S*6 configurations give sharply different solutions for formation energy and all other properties presented in Table 2 depending on size of the supercell (*L*4 *vs. L*8). For S6 in *L*4, which corresponds to dumbbell configuration with the oxygen interstitial [28], O_i-O_{reg} distance noticeably reduces, being accompanied by a marked decrease in formation energy. *Vice versa*, in the case of *L*8 the strong Al-O bonding is observed parallel with growing distances to the nearest oxygen atoms, which results in much higher formation energy. *S*2 site symmetry in $MgAl_2O_4$ bulk is characterized by tetrahedral arrangement of the pairs of Mg and O_{reg} atoms around O_i, and since their O_i-O_{reg} distance in tetrahedron in larger that in *S*6 (*L*4) configuration, energy $E_{form}^{O_i}$ of the latter is found to be smaller. The lowest formation energies correspond to the lowest site symmetry *S*1. For both *L*4 and *L*8 supercells, formation of O_i-O_{reg} split interstitial (or dumbbell) is observed ($d_{O\text{-}O}$ = 1.42-1.44 Å). This configuration is for more than 2 eV more preferable than all the others. Similar behaviour of interstitials is known also in other oxides, where the two oxygen atoms are placed around regular oxygen site in lattice, preserving site symmetry. The distance between two oxygen species is very similar to peroxide bond length.

Table 2. Closed shell (singlet) calculations on the interstitial O_i atom positioned in four different split vacant positions. The Wyckoff positions (2*b* and 4*c*) of O_i are split into 4 orbits in the 56 (*L*4) and 112 (*L*8) atom containing supercells (Fig. 1). *SP* denotes the site symmetry group possessing *P* point group operations. 1NN and 2NN denote the first and second spheres of the nearest atoms around O_i interstitial.

Supercell	*L*4	*L*8	*L*4	*L*8	*L*4	*L*8	*L*4	*L*8
Symmetry site	*S*24/*S*8 (2*b*)		*S*6 (2*b*)		*S*2 (4*c*)		*S*1 (no symmetry)	
Coordinates	(0.5 0.5 0.5) / (0 0 0.5)		(0.25 0.25 0.25)		(-0.125 -0.375 -0.375)		(0.25 0.25 0.25)	
$E_{form}^{O_i}$ energy (eV), Eq. (8)	13.7	13.0	4.4	8.6	5.07	5.14	2.31	2.51
1NN distance (Å)	4Al 1.851	4Al 1.843	O 1.352	Al 1.638	O 1.757	O 1.757	O 1.415	O 1.44
2NN distance (Å)	4O 1.942	4O 1.935	3Al 1.872	3 O 2.012	Mg 1.783	Mg 1.780	2Al 1.880	2Al 1.880
Effective O_i charge (*e*)	-0.71	-0.71	-0.60	-0.53	-0.58	-0.59	-0.61	-0.63
1NN overlap population (*e*)	0.01	-0.01	0.04	0.50	-0.136	-0.14	-0.12	-0.084
2NN overlap population (*e*)	-0.04	-0.04	0.27	-0.07	0.028	0.024	0.274	0.262

Analysis of the Mg-spinel DOS (Figure 3) shows that O_i-O_{reg} pair forms occupied band just above the top of the valence band (VB) and unoccupied band near to the bottom of conduction band (CB). The reason for that can be O-O orbital overlapping and splitting into π, π* and σ* orbitals. In the case of *S*2 configuration, overlap population reveals interaction between the two oxygen atoms. This results in two peaks of DOS just above the top of the VB. In *S*8/*S*24 configurations O_i is well-separated from other atoms and DOS shows only 2*p* electrons of isolated oxygen ~2 eV above the top of the VB. Distance between O_i and O_{reg} in *S*6 configuration is minimal, but the orbital splitting is not observed and the plot is similar to *S*8/*S*24 configuration. The possible

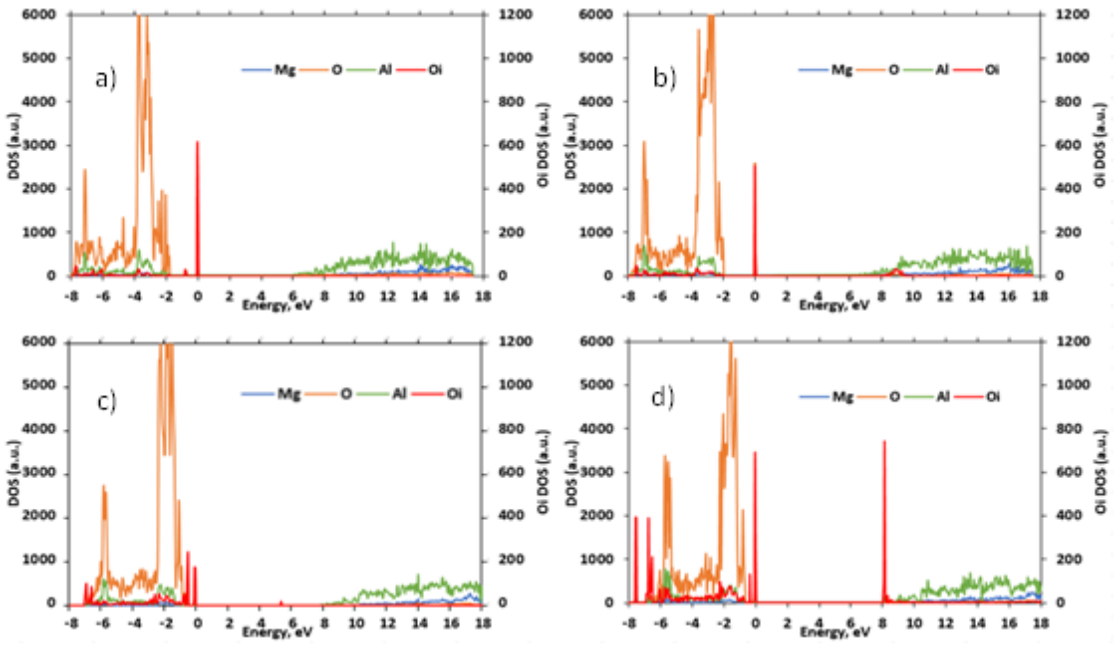

Figure 3. Calculated densities of states (DOS) for *S*24/*S*8 (a), *S*6 (b), *S*2 (c) and *S*1 (d) in *L*4 supercell. Zero energy corresponds to highest occupied band. DOS for O_i corresponds to secondary (right) y-axis.

explanation for this effect can be symmetry restriction, which results in formation energy by 1.1 eV higher than for *S*1.

4.2. Analysis of the phonon structure

In the case of defective crystal the degenerate vibrational modes defined by Eq. (9) are split. The latter depends on the point symmetry of O_i position. Three displacements (*x y z*) of interstitial oxygen generate additional vibrational modes with the symmetry depending on the interstitial oxygen point group: *S*24 (T_d) - T_2; *S*6 (C_{3v}) - A_1, E; *S*2 (C_s) - A, 2B; *S*1 (C_1) - 3A.

Table 3. The frequencies (in cm^{-1}) of the optical modes of $MgAl_2O_4$ bulk at the Γ point of the Brillouin zone of the primitive unit cell *L*1 (Fig. 1a). IR - infrared-active modes, R - Raman active modes. LO phonon frequencies are given in brackets.

Phonon modes	DFT-PW calculations [42]	Our hybrid DFT-LCAO HSE06 calculations	Experimental data [43, 44]
T_{2u}	265	269	
T_{1u} (R)	311 (319)	308 (315)	303-309
T_{2g} (R)	319	323	305-312
T_{1g}	360	362	
E_u	412	420	
E_g (R)	426	421	407-411
T_{2u}	483	484	
T_{1u} (IR)	512 (580)	503 (606)	510-533
T_{2g} (R)	570	593	666-681
T_{1u} (IR)	588 (638)	608 (646)	581
E_u	608	630	
A_{2u}	668	693	
T_{2g} (R)	682	698	
T_{1u} (IR)	698 (866)	710 (870)	680-692
A_{2u}	763	785	
A_{1g} (R)	776	796	720-790

The phonon calculations of defective $MgAl_2O_4$ crystal have been performed for supercell model *L*4 (56 atoms) and three interstitial oxygen positions *S*6 (C_{3v}), *S*2 (C_s) and *S*1 (or *S*6 with SYMREMO: C_1) (Table 3). In the first two cases, the high values of imaginary frequencies have been found: E phonon (with frequency 274 cm^{-1}) for *S*6 symmetry and two phonons of B symmetry (C_s case) with frequencies 499 cm^{-1} and 120 cm^{-1}. This means the non-stability of the models with C_{3v} and C_s point symmetries, *i.e.*, the calculated formation energies correspond to local minima of the total energy. It is seen that absolute values of imaginary frequencies decrease with the decreasing the site symmetry of the interstitial O_i from C_{3v} to C_s. After lowering the point symmetry to C_1 the imaginary frequencies disappear at all, thus confirming the stability of interstitial oxygen position with symmetry *S*1. In the latter case three additional (compared with the bulk crystal) non-degenerate phonon modes appear with frequencies: 41 cm^{-1}, 169 cm^{-1} and 1142 cm^{-1}. The Hessian eigenvector analysis for these modes gives that the first two modes can be considered as the bulk crystal modes distorted by interstitial oxygen. The third mode with the frequency 1142 cm^{-1} corresponds to the vibration of superoxide ion O^{2-} in crystal formed by the interstitial oxygen with the nearest (at distance ~1.35 Å) oxygen atom of the host crystal, *i.e.* the dumbbell structure. This conclusion follows from the analysis given for experimental data of the vibrational frequencies and the interatomic distances in free O_2 molecular system in the different charged states [48]: molecular O_2^+ dioxygenyl (1800 cm^{-1}, 1.12 Å), neutral O_2 molecule (1556 cm^{-1}, 1.21 Å) and molecular O_2^- superoxide (1143 cm^{-1}, 1.28 Å).

5. Conclusions

The site symmetry approach applied for various configurations of O_i interstitial *per L*4 and L8 supercells of $MgAl_2O_4$ spinel is based on the group-theoretical analysis of the split Wyckoff positions in the perfect crystal. When performing this analysis, we have compared five possible spatial configurations for inserting oxygen atoms into interstitial positions of spinel structure. Intuitively, the interstitial configuration highest by symmetry in the supercell model simultaneously provides the highest formation energy, while arrangement of O_i atoms in less symmetric sites of spinel lattice is essentially more preferable energetically: values of $E_{form}^{O_i}$ in the latter are found to be 5-6 times larger. However, the examination of the lowest symmetry sites *S*1 only is not enough since the low formation energy can correspond not only to C_1 symmetry, but also to a higher one (it depends also on the size and shape of supercell).

The interstitials are also unstable to the almost spontaneous transformation from high-symmetric into split interstitials (dumbbells) which are remoted from the nearest regular O_{reg} atoms by 1.42-1.44 Å. Obviously, this is a distance, typical for O_2^{2-} peroxides, whereas its charge (~1 *e*) is qualitatively similar to that of a free O_2^- superoxide. Moreover, within the SCM model, the dumbbell configuration automatically appears as a result of the automated structure optimization, making no spposition on the O_i path from the starting position of its arrangement. The calculated formation energies in these cases correspond to rather global minima of the total energy.

The analysis of the electron DOS clearly demonstrates that the dumbbell produces both the occupied states close to the top of the VB as well as the unoccupied states close to the bottom of the CB. The reason for that can be O-O orbital overlapping and splitting into π, π* and σ* orbitals.

In the case of *S*2 configuration, overlap population reveals interaction between the two oxygen atoms leading to appearance of the two DOS peaks just above the top of the VB.

As an argument in favour of dumbbell O_i-O_{reg} configuration in spinel bulk, we consider also high values of imaginary frequencies found for *S*6 symmetry and in the case of *S*2 symmetry indicating the non-stability of both interstitial models. Moreover, the absolute values of imaginary frequencies are found to be reduced with the decreasing the site symmetry of the interstitial O_i from C_{3v} to C_s. After lowering the point symmetry to C_1 the imaginary frequencies disappear at all, thus confirming the stability of interstitial oxygen position with symmetry *S*1.

Acknowledgements

This study has been carried out within the framework of the EUROfusion Consortium and has been provided funding from the Euratom research and training programme 2014-2018 under grant agreement No 633053. The authors are indebted to E.A. Kotomin, A.I. Popov and R. Vila for stimulating discussions. The views and opinions expressed herein do not necessarily reflect those of the European Commission. Calculations have been performed using both the Marconi supercomputer system at the Computational Simulation Centre (Italy) and the Computer Center of St. Petersburg State University.

References

1. Satoh, T.; Tsushima, T.; Kudo, K. A classification of normal spinel type compounds by "Ionic packing factor". *Mater. Res. Bull.* **1974**, 9(10), 1297-1300. https://doi.org/10.1016/0025-5408(74)90051-8
2. Burdett, J.K.; Price, G.D.; Price, S.L. Factors influencing solid-state structure—an analysis using pseudopotential radii structural maps. *Phys. Rev. B* **1981**, 24(6), 2903-2912. https://doi.org/10.1103/PhysRevB.24.2903
3. Ottonello, G. Energetics of multiple oxides with spinel structure. *Phys. Chem. Minerals* **1986**, 13(2), 79-90. https://doi.org/10.1007/BF00311897
4. Li, J.G.; Ikegami, T.; Lee, J.H.; Mori, T.; Yajima, Y. Synthesis of Mg–Al spinel powder via precipitation using ammonium bicarbonate as the precipitant. *J. Eur. Ceram. Soc.* **2001**, 21, 139-148. https://doi.org/10.1016/S0955-2219(00)00188-6
5. Walker, E.H.; Owens, J.W.; Etienne, M.; Walker, D. The novel low temperature synthesis of nanocrystalline $MgAl_2O_4$ spinel using "gel" precursors. *Mater. Res. Bull.* **2002**, 37, 1041-1050. https://doi.org/10.1016/S0025-5408(02)00740-7
6. Krell, A.; Klimke, J.; Hutzler, T. Advanced spinel and sub-µm Al_2O_3 for transparent armour applications. *J. Eur. Ceram. Soc*. **2009**, 29, 275-281. https://doi.org/10.1016/j.jeurceramsoc.2008.03.024
7. Matzke, H.; Rondinella, V.V.; Wiss, T. Materials research on inert matrices: a screening study. *J. Nucl. Mater*. **1999,** 274, 47-53. https://doi.org/10.1016/S0022-3115(99)00062-8
8. Clinard Jr, F.W.; Hurley, G.F.; Klaffky, R.W. Ceramics for fusion reactor applications. *Res. Mechanica*. **1983**, 8, 207-234.
9. Rébola, A; Fong, D.D.; Eastman, J.A.; Öğüt, S.; Zapol, P. First-principles study of compensation mechanisms in negatively charged $LaGaO_3$/$MgAl_2O_4$ interfaces. *Phys. Rev. B* **2013**, 87, 245117. https://doi.org/10.1103/PhysRevB.87.245117
10. Bandyopadhyay, P.K.; Summers, G.P. Luminescence and photoconductivity in magnesium aluminium spinel. *Phys. Rev. B* **1985**, 31, 2422-2426. https://doi.org/10.1103/PhysRevB.31.2422
11. Sawai, S; Uchino, T. Visible photoluminescence from $MgAl_2O_4$ spinel with cation disorder and oxygen vacancy. *J. Appl. Phys.* **2012,** 112, 103523. https://doi.org/10.1063/1.4767228
12. Voß, M.; Borgmann, D.; Wedler, G. Characterization of alumina, silica, and titania supported cobalt catalysts. *J. Catal.* **2002**, 212, 10-21. https://doi.org/10.1006/jcat.2002.3739
13. Tielens, F.; Calatayud, M.; Franco, R.; Recio, J.M.; Pérez-Ramírez, J.; Minot, C. Periodic DFT study of the structural and electronic properties of bulk $CoAl_2O_4$ spinel. *J. Phys. Chem. B.* **2006**, 110, 988-995. https://doi.org/10.1021/jp053375
14. Gusmano, G.; Montesperelli, G.; Traversa, E.; Mattogno, G. Microstructure and electrical properties of $MgAl_2O_4$ thin films for humidity sensing. *J. Am. Ceram. Soc.* **1993,** 76, 743-750. https://doi.org/10.1111/j.1151-2916.1993.tb03669.x
15. Xu, Y.N.; Ching, W.Y. Self-consistent band structures, charge distributions, and optical-absorption spectra in MgO, α-Al_2O_3, and $MgAl_2O_4$. *Phys. Rev*. B **1991**, 43, 4461-4472. https://doi.org/10.1103/PhysRevB.43.4461

16. Khenata, R.; Sahnoun, M.; Baltache, H.; Rérat, M.; Reshak, A.H.; Al-Douri, Y.; Bouhafs, B. Full-potential calculations of structural, elastic and electronic properties of $MgAl_2O_4$ and $ZnAl_2O_4$ compounds. *Phys. Lett. A* **2005**, 344, 271-279. https://doi.org/10.1016/j.physleta.2005.06.043
17. Hosseini, S.M. Structural, electronic and optical properties of spinel $MgAl_2O_4$ oxide. *Phys. Status Solidi B* **2008**, 245, 2800-2807. https://doi.org/10.1002/pssb.200844142
18. Jiang, S.; Lu, T.; Long, Y.l.; Chen, J. Ab initio many-body study of the electronic and optical properties of $MgAl_2O_4$ spinel. *J. Appl. Phys.* **2012**, 111, 043516. https://doi.org/10.1063/1.3686727
19. Brik, M.G.; Suchocki, A.; Kamińska, A. Lattice parameters and stability of the spinel compounds in relation to the ionic radii and electronegativities of constituting chemical elements. *Inorg. Chem.* **2014**, 53, 5088-5099. https://doi.org/10.1021/ic500200a
20. Borges, P.D.; Cott. J.; Pinto, F.G.; Tronto. J.; Scolfaro, L. Native defects as sources of optical transitions in $MgAl_2O_4$ spinel. *Mater. Res. Express* **2016**, 3, 076202. https://doi.org/10.1088/2053-1591/3/7/076202
21. Smith, R.; Bacorisen, D.; Uberuaga, B.P.; Sickafus, K.E.; Ball, J.A.; Grimes, R.W. Dynamical simulations of radiation damage in magnesium aluminate spinel, $MgAl_2O_4$. *J. Phys. Condens. Matter* **2005**, 17, 875-891. https://doi.org/10.1088/0953-8984/17/6/008
22. Łodziana, Z.; Piechota, J. *Ab initio* thermodynamic properties of point defects and O-vacancy diffusion in Mg spinels. *Phys. Rev. B.* **2006**, 74, 184117. https://doi.org/10.1103/PhysRevB.74.184117
23. Uberuaga, B.P.; Bacorisen, D.; Smith. R.; Ball, J.A.; Grimes, R.W.; Voter, A.F.; Sickafus, K.E. Defect kinetics in spinels: Long-time simulations of $MgAl_2O_4$, $MgGa_2O_4$, and $MgIn_2O_4$. *Phys. Rev. B.* **2007**, 75, 104116. https://doi.org/10.1103/PhysRevB.75.104116
24. Ball, J.A.; Murphy, S.T.; Grimes, R.W.; Bacorisen, D.; Smith, R. Uberuaga, B.P.; Sickafus, K.E. Defect processes in $MgAl_2O_4$ spinel. *Solid State Sci.* **2008**, 10, 717-724. https://doi.org/10.1016/j.solidstatesciences.2007.04.005
25. Gilbert. C,A.; Smith, R.; Kenny, S.D.; Murphy, S.T.; Grimes, R.W.; Ball, J.A. A theoretical study of intrinsic point defects and defect clusters in magnesium aluminate spinel. *J. Phys.: Condens. Matter*. 2009, **17,** 275406. https://doi.org/10.1088/0953-8984/21/27/275406
26. Paudel, T.R.; Zakutayev, A.; Lany, S.; d'Avezac, M.; Zunger, A. Doping rules and doping prototypes in A_2BO_4 spinel oxides. *Adv. Funct. Mater.* **2011**, 21, 4493-4501. https://doi.org/10.1002/adfm.201101469
27. Evarestov, R.A.; Platonenko, A.; Gryaznov, D.; Zhukovskii, Y.F.; Kotomin, E.A. First-principles calculations of oxygen interstitials in corundum: a site symmetry approach. *Phys. Chem. Chem. Phys.* **2017**, 19, 25245-25251. https://doi.org/10.1039/C7CP04045H
28. Evarestov, R.A.; Jacobs, P.W.M.; Leko, A.V. Oxygen interstitials in magnesium oxide: A band-model study. *Phys. Rev. B* **1996**, 54, 8969-8972. https://doi.org/10.1103/PhysRevB.54.8969
29. http://www.cryst.ehu.es/ Bilbao Crystallographic Server (BCS).
30. Evarestov, R.A.; Smirnov, V.P. Symmetrical transformation of basic translation vectors in the supercell model of imperfect crystals and in the theory of special points of the Brillouin zone. *J. Phys.: Condens. Matter* **1997**, 9, 3023-3031. https://doi.org/10.1088/0953-8984/9/14/016
31. Heyd, J.; Scuseria, G.E.; Ernzerhof, M. Hybrid functionals based on a screened Coulomb potential. *J. Chem. Phys.* **2003**, 118, 8207-8215. https://doi.org/10.1063/1.1564060
32. Dovesi, R.; Saunders, V. R.; Roetti, C.; Orlando, R.; Zicovich-Wilson, C. M.; Pascale, F.; Civalleri, B.; Doll, K.; Harrison, N. M.; Bush, I. J.; D'Arco, P.; Llunell, M.; Causà, M.; Noël, Y.; Maschio, L.; Erba, A.; Rerat, M.; Casassa, S. *CRYSTAL17 User's Manual*. University of Torino: Torino, **2017**.
33. Baima, J.; Erba, A.; Rérat, M.; Orlando, R.; Dovesi, R.; Beryllium oxide nanotubes and their connection to the flat monolayer. *J. Phys. Chem. C* **2013**, 117, 12864-12872. https://doi.org/10.1021/jp402340z
34. McCarthy, M.I.; Harrison, N.M. Ab initio determination of the bulk properties of MgO. *Phys. Rev. B* **1994**, 49, 8574-8582. https://doi.org/10.1103/PhysRevB.49.8574
35. Causà, M.; Dovesi, R.; Roetti, C. Pseudopotential Hartree-Fock study of seventeen III-V and IV-IV semiconductors. *Phys. Rev. B* **1991**, 43, 11937-11943. https://doi.org/10.1103/PhysRevB.43.11937
36. Monkhorst, H.J.; Pack, J.D. Special points for Brillouin-zone integrations. *Phys. Rev. B.* **1976**, 13, 5188-5192. https://doi/10.1103/PhysRevB.13.5188
37. O'Neill, H.S.; Navrotsky, A. Simple spinels; crystallographic parameters, cation radii, lattice energies, and cation distribution. *Amer. Mineralogist* **1983**, 68, 181-194.
38. Ishii, M.; Hiraishi, J.; Yamanaka, T. Structure and lattice vibrations of Mg-Al spinel solid solution. *Phys. Chem. Minerals*. **1982**, 8, 64-68. https://doi.org/10.1007/BF00309015
39. Bortz, M.L.; French, R.H.; Jones, D.J.; Kasowski, R.V.; Ohuchi, F.S. Temperature dependence of the electronic structure of oxides: MgO, $MgAl_2O_4$ and Al_2O_3. *Phys. Scr.* **1990**, 41, 537-541. https://doi.org/10.1088/0031-8949/41/4/036
40. Suzuki, I.; Ohno, I.; Anderson, O.L. Harmonic and anharmonic properties of spinel $MgAl_2O_4$. *Amer. Mineralogist* **2000**, 85, 304-311. https://doi.org/10.2138/am-2000-2-307

41. Mulliken, R.S. Electronic population analysis on LCAO–MO molecular wave functions. I. *J. Chem. Phys.* **1955**, 23, 1833-1840. https://doi.org/10.1063/1.1740588
42. Evarestov, R.A.; Losev, M.V. All-electron LCAO calculations of the LiF crystal phonon spectrum: Influence of the basis set, the exchange-correlation functional, and the supercell size. *J. Comput. Chem*. **2009**, 30, 2645-2655. https://doi.org/10.1002/jcc.21259
43. Pascale, F.; Zicovich-Wilson, C.M.; Lopez Gejo, F.; Civalleri, B.; Orlando, R.; Dovesi, R. The calculation of the vibrational frequencies of crystalline compounds and its implementation in the CRYSTAL code. *J. Comput. Chem*. **2004,** 25, 888-897. http://doi.org/10.1002/jcc.20019
44. Zicovich-Wilson, C.M.; Pascale, F.; Roetti, C.; Saunders, V.R.; Orlando, R.; Dovesi, R. Calculation of the vibration frequencies of α-quartz: The effect of Hamiltonian and basis set. *J. Comput. Chem*. **2004,** 25, 1873-1881. https://doi.org/10.1002/jcc.20120
45. De Wijs, G.A.; Fang. C.M.; Kresse. G. First-principles calculation of the phonon spectrum of $MgAl_2O_4$ spinel. *Phys. Rev. B.* **2002**, 65, 094305. https://doi.org/10.1103/PhysRevB.65.094305
46. Slotznick, S.P.; Shim, S.H. In situ Raman spectroscopy measurements of $MgAl_2O_4$ spinel up to 1400 C. *Amer. Mineralogist.* **2008,** 93, 470-476. https://doi.org/10.2138/am.2008.2687
47. Boguslavska, N.N.; Venger, E.F.; Vernidub, N.M.; Pasechnik, Y.A.; Shportko, K.V. Reststrahlen spectroscopy of $MgAl_2O_4$ spinel. *Semicond. Phys. Quantum Electron. Optoelectron.* **2002**, 5, 95–100.
48. Shamir, J.; Binenboym, J.; Claassen, H.H.; The vibrational frequency of the oxygen molecule (O_2+) cation. *J. Amer. Chem. Soc.* **1968,** 6223-6224. https://doi.org/10.1021/ja01024a054

Institute of Solid State Physics, University of Latvia as the Center of Excellence has received funding from the European Union's Horizon 2020 Framework Programme H2020-WIDESPREAD-01-2016-2017-TeamingPhase2 under grant agreement No. 739508, project CAMART²